Nano-Micro Letters

e-ISSN 2150-5551
CN 31-2103/TB

ARTICLE

https://doi.org/10.1007/s40820-024-01497-z

"Zero-Strain" $NiNb_2O_6$ Fibers for All-Climate Lithium Storage

Yan Zhao[1,2], Qiang Yuan[2], Liting Yang[3], Guisheng Liang[3], Yifeng Cheng[4], Limin Wu[5] ✉, Chunfu Lin[1,2] ✉, Renchao Che[1,3,4] ✉

Cite as
Nano-Micro Lett.
(2025) 17:15

Received: 4 May 2024
Accepted: 5 August 2024
© The Author(s) 2024

HIGHLIGHTS

- "Zero-strain" $NiNb_2O_6$ fibers with nanosized primary particles are explored as an all-climate anode material with comprehensively good Li^+-storage properties.
- The almost completely opposite volume changes of electrochemical inactive NiO_6 octahedra and active NbO_6 octahedra are achieved through reversible O movement, leading to the "zero-strain" behavior of $NiNb_2O_6$ with minor unit-cell-volume change and excellent cyclability in a broad temperature range.
- The gained insight can provide guide for the exploration of high-performance energy-storage materials working at harsh temperatures.

ABSTRACT Niobates are promising all-climate Li^+-storage anode material due to their fast charge transport, large specific capacities, and resistance to electrolyte reaction. However, their moderate unit-cell-volume expansion (generally 5%–10%) during Li^+ storage causes unsatisfactory long-term cyclability. Here, "zero-strain" $NiNb_2O_6$ fibers are explored as a new anode material with comprehensively good electrochemical properties. During Li^+ storage, the expansion of electrochemical inactive NiO_6 octahedra almost fully offsets the shrinkage of active NbO_6 octahedra through reversible O movement. Such superior volume-accommodation capability of the NiO_6 layers guarantees the "zero-strain" behavior of $NiNb_2O_6$ in a broad temperature range (0.53%//0.51%//0.74% at 25//−10//60 °C), leading to the excellent cyclability of the $NiNb_2O_6$ fibers (92.8%//99.2% // 91.1% capacity retention after 1000//2000//1000 cycles at 10C and 25//−10//60 °C). This $NiNb_2O_6$ material further exhibits a large reversible capacity (300//184//318 mAh g^{-1} at 0.1C and 25//−10//60 °C) and outstanding rate performance (10 to 0.5C capacity percentage of 64.3%//50.0%//65.4% at 25//−10//60 °C). Therefore, the $NiNb_2O_6$ fibers are especially suitable for large-capacity, fast-charging, long-life, and all-climate lithium-ion batteries.

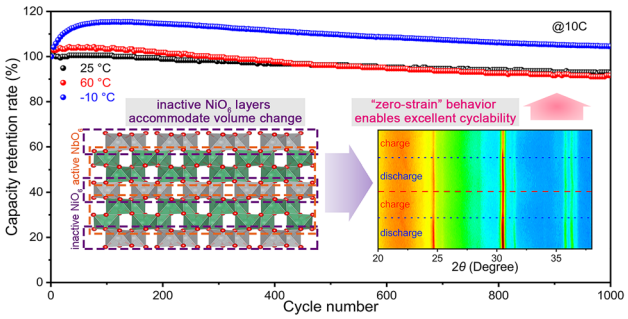

KEYWORDS $NiNb_2O_6$ porous fiber; "Zero-strain" mechanism; Electrochemical property; Harsh-temperature operation; *Operando* characterization

✉ Limin Wu, wlm@imu.edu.cn; Chunfu Lin, linchunfu@dhu.edu.cn; Renchao Che, rcche@fudan.edu.cn
[1] College of Physics, Donghua University, Shanghai 201620, People's Republic of China
[2] School of Materials Science and Engineering, Institute of Materials for Energy and Environment, Qingdao University, Qingdao 266071, People's Republic of China
[3] Laboratory of Advanced Materials, Shanghai Key Laboratory of Molecular Catalysis and Innovative Materials, Academy for Engineering & Technology, Fudan University, Shanghai 200438, People's Republic of China
[4] Zhejiang Laboratory, Hangzhou 311100, People's Republic of China
[5] Inner Mongolia University, Hohhot 010021, People's Republic of China

Published online: 27 September 2024

1 Introduction

Lithium-ion batteries (LIBs) are very popular electrochemical energy-storage devices. However, the current LIBs still have limitations in terms of energy density, power density, cyclability, safety, and temperature adaptability [1–5]. Especially, both low and high temperatures reduce the energy and power densities of LIBs, rendering them less practical in high altitude/latitude and hot tropical/summer regions [6–9]. Graphite, the most widely-used anode material in current LIBs, possesses a large theoretical capacity (372 mAh g^{-1}), excellent electronic conductivity, and low cost, but suffers from a safe problem arising from the easy lithium-dendrite formation [10]. Additionally, high temperatures cause excessive Li^+ intercalation in graphite, resulting in severe particle cracks and fast capacity decay [11, 12]. At low temperatures, graphite experiences significant increase in charge transfer resistance and notable decrease in Li^+ diffusivity, which lead to severe rate-performance fade [13, 14]. $Li_4Ti_5O_{12}$, another commercial anode material, demonstrates excellent rate capability and cyclability after properly modified [15]. However, $Li_4Ti_5O_{12}$ suffers from several issues, including the very limited theoretical capacity (only 175 mAh g^{-1}), intensive reaction of Ti^{4+} with electrolyte at high temperatures, and slow Li^+ diffusivity at low temperatures [15–17].

The recently-developed niobate anode materials provide a viable solution to the aforementioned challenges [12, 18–21]. They possess open crystal structures and multiple lithiation sites with electrochemical-active Nb ions [22–30]. These advantages enable superior charge-transport capability and large-capacity Li^+ storage over multiple discharge–charge cycles. Additionally, they exhibit resistance to electrolyte reaction, low polarization, and fast ion migration, rendering them suitable for harsh-condition applications [31, 32]. However, their long-term cyclability is unsatisfactory, mainly due to their moderate unit-cell-volume expansion (generally 5%–10%) after lithiation [33]. In this regard, "zero-strain" niobates with minor unit-cell-volume change of < 1% have gained much research interest, which can show minor stress generated during lithiation, thereby avoiding microcrack formation and enabling excellent cyclability [34–36]. Here, zero-strain means no unit-cell-volume change during electrochemical reaction, and the further use of quotes means tiny unit-cell-volume change of < 1%. In 2021, Xia et al. reported $NiNb_2O_6$ submicron particles (averaging at 680 nm) with a "zero-strain" potential through solid-state reaction [37]. This material had high rate performance (10 to 0.5C capacity percentage of 57.4%) and good cyclability (capacity retention of 92.0% after 2500 cycles at 10C) at 25 °C, demonstrating is practicability. To commercialize $NiNb_2O_6$, however, its electrochemical properties need to be further improved, its harsh-temperature operation needs to be investigated, and its "zero-strain" behavior and mechanism need to be clarified.

In this work, we successfully synthesize $NiNb_2O_6$ fibers with primary particles of only 50–100 nm by electrospinning, improving the reversible capacity and rate performance of $NiNb_2O_6$. The maximum unit-cell-volume expansion of $NiNb_2O_6$ is determined for the first time (only + 0.53%// + 0.51%// + 0.74% at 25// − 10//60 °C), and its "zero-strain" behavior in the broad temperature range is identified. During lithiation, the expansion of electrochemical inactive NiO_6 octahedra almost fully offsets the shrinkage of active NbO_6 octahedra through reversible O movement, resulting in its "zero-strain" structure stability and excellent cyclability (92.8%//99.2%//91.1% capacity retention after 1000//2000//1000 cycles at 10C and 25// − 10//60 °C). Furthermore, the $NiNb_2O_6$ fibers exhibit a large reversible capacity (300//184//318 mAh g^{-1} at 0.1C and 25// − 10//60 °C) and outstanding rate performance (10 to 0.5C capacity percentage of 64.3%//50.0%//65.4% at 25// − 10//60 °C) in the broad temperature range. Therefore, the good practicability of our modified $NiNb_2O_6$ material in all-climate LIBs is fully revealed.

2 Experimental Section

2.1 Material Synthesis

0.02 mol of $NbCl_5$ (99.9%, Macklin) was thoroughly mixed with 10 mL of N, N-dimethylformamide (DMF), which was stirred until a translucent orange solution was formed. 0.01 mol of $NiCl_2{\cdot}6H_2O$ (99.9%, Macklin) was added to this solution and stirred until the clear solution turned green in color. Then, 1.0 g of polyvinylpyrrolidone (M_w = 1,300,000, Macklin) was dissolved in this solution with stirring, forming the electrospinning solution. The electrospinning experiment was conducted on a commercial electrospinning machine (TL-Pro-BM). The electrospinning potential, pumping rate, and distance between the syringe tip and film collector were set to be 16 kV, 0.6 mL h^{-1}, and 20 cm, respectively. The electrospun film was heated at 850 °C for 4 h in air, resulting in the formation of $NiNb_2O_6$ fibers.

© The authors
https://doi.org/10.1007/s40820-024-01497-z

2.2 Material Characterizations

The crystal structure of $NiNb_2O_6$ was analyzed on an X-ray diffractometer (Rigaku Smart Lab) with Cu Kα radiation. The General Structure Analysis System (GSAS) Program was employed to Rietveld refine the obtained XRD patterns [38]. Morphology observations were conducted using field emission scanning electron microscopy (FESEM, JEOL JSM-7800F) equipped with energy dispersive spectroscopy (EDS, OXFORD X-Max) and high-resolution transmission electron microscopy (HRTEM, JEOL JEM-2100Plus). The Brunauer–Emmett–Teller (BET) model was used to calculate the specific surface area of the $NiNb_2O_6$ fibers based on the N_2 adsorption data recorded on an ASAP 2460 surface area analyzer. The Barrett–Joyner–Halenda (BJH) model was employed to compute the pore-size-distribution curve from the desorption branch. The ultraviolet–visible (UV–Vis) absorption spectrum of $NiNb_2O_6$ was recorded using a U-3900H spectrophotometer. The electronic conductivity of $NiNb_2O_6$ was tested by employing a two-probe direct current method on a compacted $NiNb_2O_6$ pellet. The valence changes of $NiNb_2O_6$ on cast electrodes were analyzed using X-ray photoelectron spectroscopy (XPS) on a PHI5000 Versa probe III system. In an Ar-filled glove box, the $NiNb_2O_6$ electrodes at different discharge/charge states were disassembled from the coin cells, and then washed with dimethyl carbonate (DMC). After fully dried, the $NiNb_2O_6$ electrodes were sealed in an XPS sample stage before the XPS examinations.

2.3 Electrochemical Characterizations

For the preparation of the working electrodes for half cells, the synthesized $NiNb_2O_6$ powder (active material, 75 wt%), Super-P conductive carbon (for conductivity, 15 wt%), polyvinylidene fluoride (binder, 10 wt%), and N-methyl-2-pyrrolidone (solvent) were mixed in a bottle and stirred for 4 h to form a slurry. The slurry was then cast into copper (Cu) foils with a loading of ~ 1.5 mg cm^{-2}, which were fully dried in a vacuum oven at 110 °C for 12 h. The electrochemical tests were conducted on CR2016-type half coin cells assembled in an Ar-filling glove box, with Celgard® 2325 microporous polypropylene films as separators, Li-metal foils as counter electrodes, and 1 M $LiPF_6$ in a 1:1:1 volume ratio of ethylene carbonate, diethylene carbonate, and dimethyl carbonate as electrolyte. The galvanostatic intermittent titration technique (GITT) and galvanostatic charge–discharge (GCD) tests within 1.0–3.0 V were performed using a Neware CT-3008 battery tester at different temperatures controlled in an LRHS-101C temperature-variable cryostat system, and cyclic voltammetry (CV) and electrochemical impedance spectroscopy (EIS) experiments were further performed using a Gamry Interface1010E electrochemical workstation.

2.4 *Operando* Characterizations

Operando XRD experiments were carried out to study the lattice-parameter variations of $NiNb_2O_6$ during electrochemical reactions at various temperatures of 25, − 10, and 60 °C. The construction process of the in-situ XRD cell at 25 °C followed the same procedure as that of the half cells, except that the $NiNb_2O_6$-based composite film was peeled off from the Cu foil and then coated on a beryllium (Be) plate. This Be plate served as both the X-ray penetration window and current collector within a specially designed module (LIB-XRD, Beijing Scistar Technology). To maintain the desired operating temperature at − 10 or 60 °C, the module (LHTXRD-LN, Beijing Scistar Technology) incorporated an X-ray penetration polyetheretherketone (PEEK) dome and a temperature-control unit [39].

The *operando* TEM test was carried out to track the real-time microstructure changes of the $NiNb_2O_6$ fibers during lithiation and delithiation using a specially-designed electrochemical holder from the X-mech Center in Zhejiang University, which simulated the operation of a half cell [18]. The working electrode was $NiNb_2O_6$ fibers on a W wire, and the counter electrode was Li metal with naturally-formed Li_2O coating on another W wire. The $Li \rightarrow Li_2O \rightarrow NiNb_2O_6$ lithiation process was observed when the two electrodes were in contact and a proper voltage was applied.

3 Results and Discussion

3.1 Structures and Physico-Chemical Characterizations

The XRD pattern of the $NiNb_2O_6$ sample is successfully refined by using the Rietveld method with a small residual value (R_{wp} = 4.48%, Fig. 1a) [38]. $NiNb_2O_6$ crystallizes in an orthorhombic crystal structure with a *Pbcn* space group. Its main characteristic peaks are located at the Bragg angles of 24.7° and 30.5°, corresponding to its (310) and (311) crystallographic planes (PDF No. 01-072-0481). Its

lattice parameters are determined to be $a = 14.033134(57)$ Å, $b = 5.685842(5)$ Å, $c = 5.021448(79)$ Å, and $V = 400.662(75)$ Å^3. In its orthogonal structure, each Ni/Nb ion is surrounded by six O^{2-} ions to form a corner-shared octahedron (Fig. 1b). Along the *a*-axis direction, NiO_6 and NbO_6 layers are alternately arranged, forming a stable layered structure with wide channels, which can be conductive to Li^+ transport and reduce the unit-cell-volume change caused by Li^+ insertion/extraction. The corner-shared NbO_6 octahedra and NiO_6 octahedra are serrated along the *b*-axis direction. Clearly, the main Li^+ diffusion direction is along the *c*-axis direction [37].

The $NiNb_2O_6$ sample has a morphology of fibers with primary-particle sizes of 50–100 nm and a large BET specific surface area of 8.35 $m^2\ g^{-1}$ (Figs. 1c, d and S1). The hierarchical pore sizes of the $NiNb_2O_6$ fibers are centered at ~ 50 and ~ 20 nm, which correspond to the inter-fiber and inter-particle pores, respectively. The well-defined lattice spacing of 0.360 nm (Fig. 1e) and the corresponding fast Fourier transform (FFT, Fig. 1e *inset*) match with the (310) plane of $NiNb_2O_6$. The homogeneous distributions of Ni, Nb, and O (Fig. 1f) confirm the high purity and uniformity of this $NiNb_2O_6$ material. $NiNb_2O_6$ exhibits a small bandgap of 2.50 eV from its UV–vis absorption spectrum (Fig. 1g), with a tested electronic conductivity reaching 2.2×10^{-8} S cm^{-1}.

3.2 Li^+-Storage Properties

From the first three-cycle GCD curves of the $NiNb_2O_6$/Li half cell recorded within a safe potential range of 1.0–3.0 V

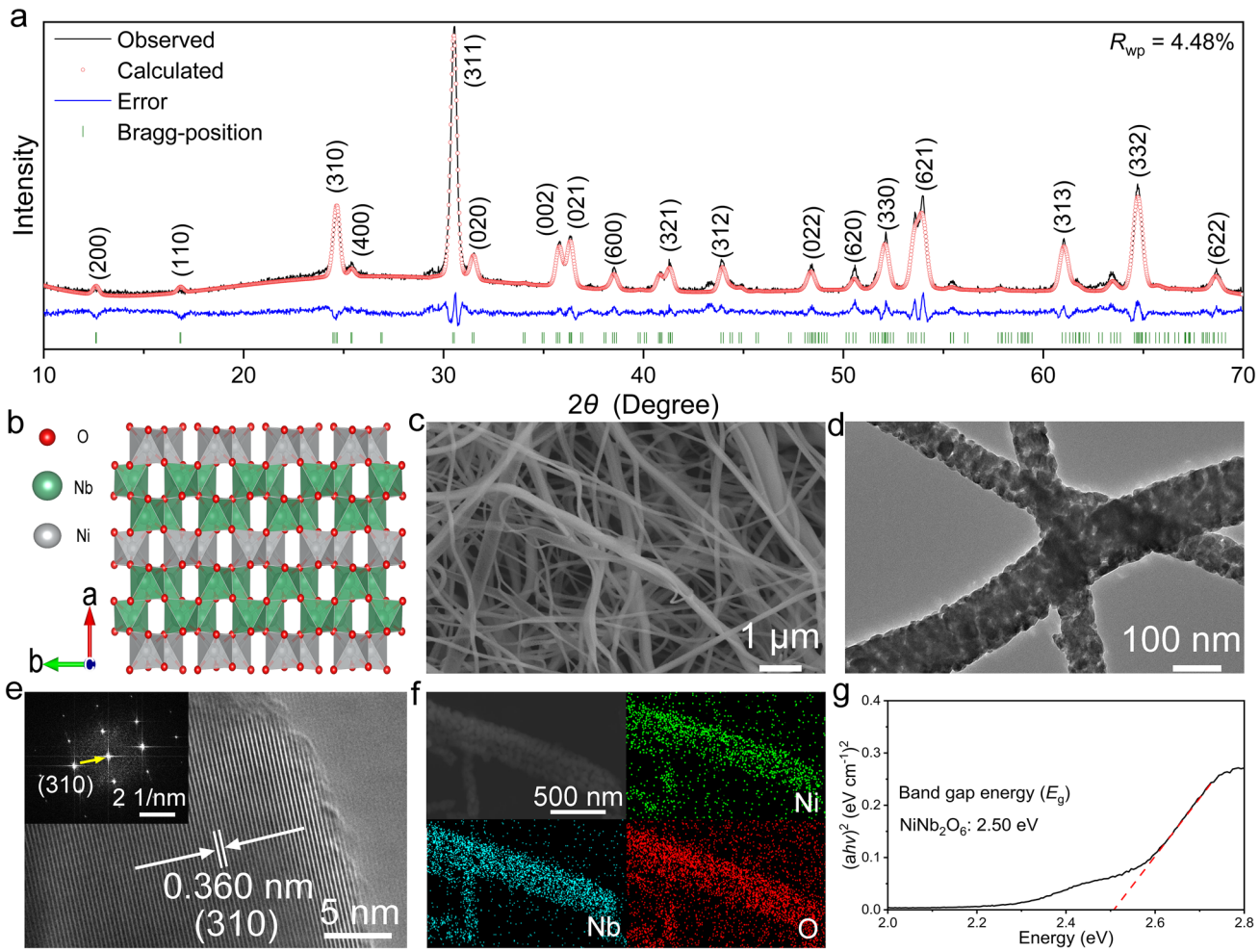

Fig. 1 Physico-chemical characterizations of $NiNb_2O_6$ fibers. **a** XRD pattern. **b** Crystal structure viewed along *c* axis. **c** FESEM image. **d** TEM image. **e** HRTEM image (*inset*: FFT). **f** EDX mapping images. **g** Evolution of optical bandgap based on UV–vis absorption spectrum. (Color figure online)

© The authors
https://doi.org/10.1007/s40820-024-01497-z

at 0.1C (Fig. S2a), it can be found that the first discharge curve shows a sequence of very fast drop (> 1.7 V) → slow drop (1.7–1.2 V) → plateau (1.2–1.3 V, phase transformation) → fast drop (< 1.2 V), whereas the second and third discharge curves follow a different sequence of very fast drop (> 2.5 V) → slow drop (2.5–1.3 V) → fast drop (< 1.3 V). The charge-curve shapes are almost fully reversible to the discharge-curve ones, except for the first one. This curve discrepancy is primarily attributed to the phase transformation of $NiNb_2O_6$ only occurring during initial lithiation. The $NiNb_2O_6$ fibers deliver a large reversible capacity of 300 mAh g^{-1} in the first cycle, approaching its theoretical capacity (315 mAh g^{-1} based on $Nb^{5+} \leftrightarrow Nb^{3+}$). At 0.5C, 1C, 2C, 5C, and 10C, large reversible capacities of 255, 226, 204, 181, and 164 mAh g^{-1} are retained, respectively (Fig. 2a, b). The resulting 10 to 0.5C capacity percentage is as large as 64.3%, which outperforms that of the previously-reported $NiNb_2O_6$ microparticles (57.4%) [37]. The data fully demonstrate the outstanding rate performance of our $NiNb_2O_6$ material. The higher activity of our $NiNb_2O_6$ material is undoubtedly due to its smaller primary particles, which enables larger electrochemical-reaction area. Meanwhile, its cyclability is also outstanding, retaining high capacity retention of 92.8% at 10C after 1000 cycles (Fig. 2c). The Nyquist plots of the $NiNb_2O_6$/Li half cell (Fig. S3) reveal that the charge-transfer resistance decreases with cycling. Such continuous activation also indicates the outstanding cyclability. Furthermore, the $LiFePO_4$/$NiNb_2O_6$ full cell also exhibits good electrochemical properties (Fig. S4a, b). Especially, its reversible capacity (212 mAh g^{-1} at 1C) is 100 and 60 mAh g^{-1} larger than that of the $LiFePO_4$/T-Nb_2O_5 and $LiFePO_4$/$Li_4Ti_5O_{12}$ full cells, respectively (Fig. S4c–f). These desirable electrochemical properties of the $NiNb_2O_6$ fibers are superior to those of most intercalation-type anode materials previously reported (Table S1).

At − 10 °C, the first discharge curve of $NiNb_2O_6$ significantly differs from that at 25 °C, with the disappearance of the plateau stage (phase transformation) at 1.0–3.0 V (Fig. S2b). The reason for this change might be attributed to the lowered ion motion at low temperatures, which inhibits the phase transformation [40–42]. However, $NiNb_2O_6$ still has a satisfactory reversible capacity of 184 mAh g^{-1} at 0.1C (Fig. S2e), 62% of that at 25 °C. In contrast, the popular $Li_4Ti_5O_{12}$ nanoparticles only exhibit a corresponding percentage of only 49% [43]. The rate performance of $NiNb_2O_6$ at − 10 °C retains high, with a 10 to 0.5C capacity percentage of 50.0% (Fig. 2d, e). In addition, the cyclability at − 10 °C is even better than that at 25 °C, exhibiting ultra-high capacity retention of 99.2% at 10C after 2000 cycles (Fig. 2f).

At 60 °C, $NiNb_2O_6$ delivers a 6% larger reversible capacity (318 mAh g^{-1} at 0.1C) and 1.1% larger 10 to 0.5C capacity percentage (65.4%) than those at 25 °C (Figs. S2c and 2g, h), undoubtedly due to the enhanced electrochemical kinetics. Importantly, it still retains high capacity retention of 91.1% at 10C after 1000 cycles (Fig. 2i). In contrast, the corresponding percentages of commercial graphite microparticles and $Li_4Ti_5O_{12}$ porous microspheres at the same elevated temperature are respectively only 36.7% after 1000 cycles at 10C and 20.9% after 500 cycles at 5C [12, 44]. To sum up, the $NiNb_2O_6$ fibers have comprehensively good electrochemical properties over a broad temperature range, becoming a practical anode material for all-climate LIBs.

3.3 Electrochemical-Reaction Mechanisms

The XPS peaks of pristine $NiNb_2O_6$ (Fig. S5d) are located at 210.5 and 207.8 eV, matching with the Nb-3$d_{3/2}$ and Nb-3$d_{5/2}$ of Nb^{5+}, respectively [45, 46]. At the discharge state of 25 °C (1.0 V, Fig. 3a), the peaks at 208.8 and 206.1 eV correspond to Nb^{4+} (33%), and the peaks at 206.9 and 204.2 eV are attributed to Nb^{3+} (67%) [47, 48]. Upon reaching the fully charged state, the valence state of Nb is restored to its original Nb^{5+} configuration (Fig. S5g). Therefore, the active Nb^{4+}/Nb^{5+} and Nb^{3+}/Nb^{4+} redox couples in $NiNb_2O_6$ are confirmed. The proportion of Nb^{3+} decreases to 20% at − 10 °C, but increases to 74% at 60 °C (Figs. 3b, c; S3e, f, h, i). These two percentage variations can be ascribed to the enhanced electrochemical kinetics at elevated temperatures. In contrast, the binding energies of Ni-2$p_{3/2}$ (856.2 eV) and Ni-2$p_{1/2}$ (873.8 eV) remain unchanged at different discharged/charged states (Fig. S5a–c) [49], indicating the very stable Ni^{2+} ions during discharge/charge, as expected.

The first-cycle (0.2 mV s^{-1}, Fig. S6a) and first four-cycle (0.4 mV s^{-1}, Fig. S6d) CV curves of the $NiNb_2O_6$/Li half-cell are displayed at 25 °C. The redox reactions involving Nb^{4+}/Nb^{5+} and Nb^{3+}/Nb^{4+} couples exhibit weak cathodic // anodic peaks at 1.71//1.77 V and intensive peaks at 1.37//1.49 V, suggesting the fast reduction of Nb^{5+} to Nb^{4+} and a significant amount of Nb^{4+} to Nb^{3+} [19, 45, 46]. These findings match well with the XPS analysis during discharge at 1.0 V. The CV curves show slight peak shifts at large sweeping rates, demonstrating small electrode polarization (Fig. 3d). At − 10 °C, the peak intensities are lower at all the

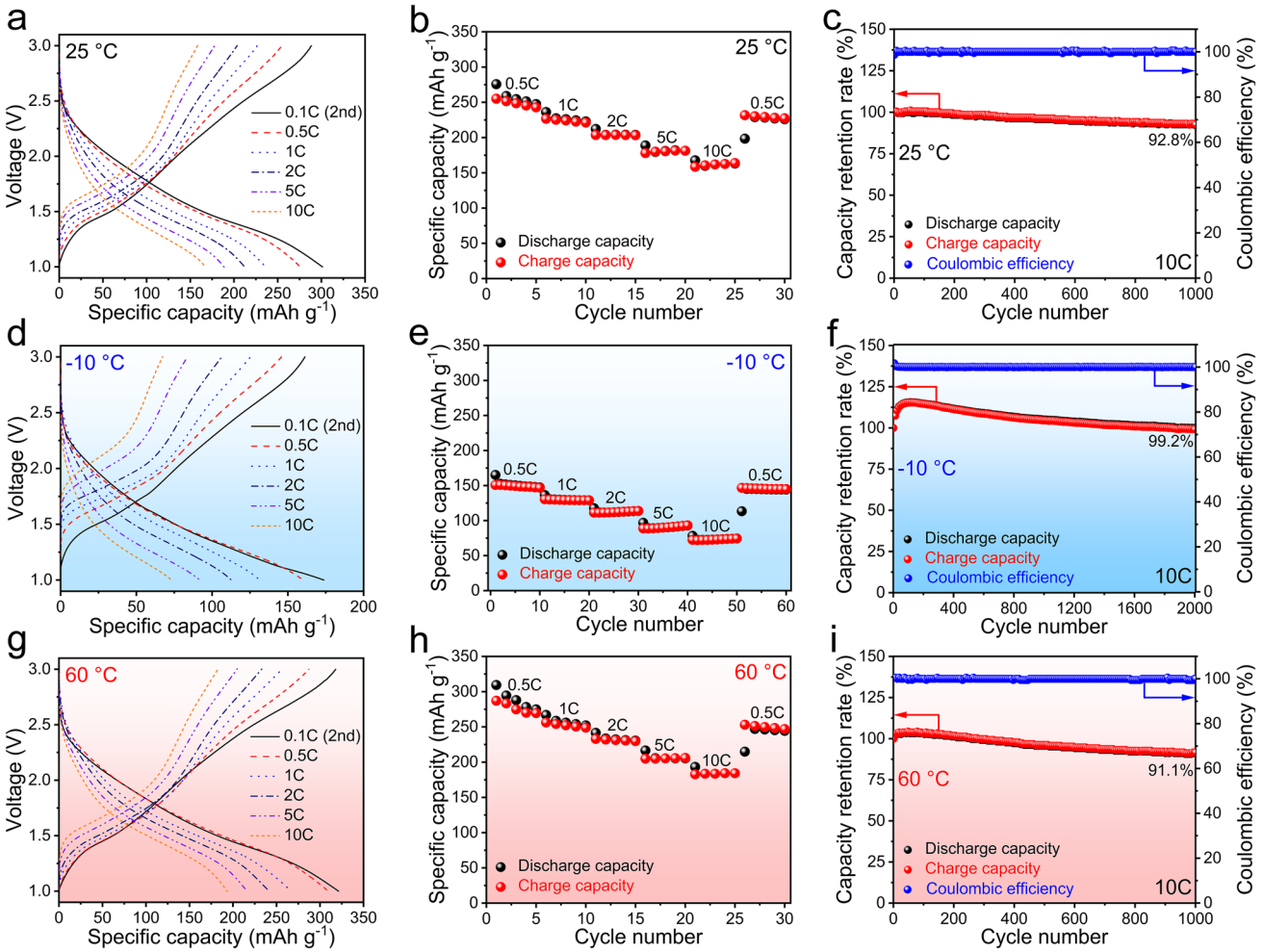

Fig. 2 Electrochemical properties of $NiNb_2O_6$ fibers at different temperatures. **a** GCD profiles at different current rates, **b** rate performance, **c** cyclability (after rate-performance test) of $NiNb_2O_6$/Li half-cell at 25 °C, **d** GCD profiles at different current rates, **e** rate performance, **f** cyclability (after rate-performance test) of $NiNb_2O_6$/Li half-cell at − 10 °C, **g** GCD profiles at different current rates, **h** rate performance, **i** cyclability (after rate-performance test) of $NiNb_2O_6$/Li half-cell at 60 °C. (Color figure online)

sweep rates, and the peaks become broader with increasing the sweep rate (Figs. 3e and S4e). At 60 °C, the peak intensities observed during the first four cycles at 0.4 mV s^{-1} are ~ 30% higher than that at 25 °C (Fig. S6f), while the results at 0.4–1.1 mV s^{-1} show a similarity to those at 25 °C (Fig. 3f). The increased polarization at the low temperature is mainly ascribed to the reduced electrical conductivity of the active material, decreased rates of ion migration, and constrained capability of charge transfer [19]. Conversely, these issues are not prevalent in high-temperature environments, thereby mitigating the polarization problem.

The Li^+ diffusivity of the $NiNb_2O_6$ fibers at various temperatures and lithiation/delithiation states is investigated through GITT (Fig. S7) [50]. At 25 °C, the average Li^+ diffusion coefficients during lithiation and delithiation respectively reach 8.1×10^{-13} and 1.4×10^{-12} cm^2 s^{-1} (Fig. 3g). At − 10 °C, the values decrease by only ~ 50% (Fig. 3h), reaching 4.5×10^{-13} cm^2 s^{-1} (lithiation) and 7.7×10^{-13} cm^2 s^{-1} (delithiation). However, larger values of 8.2×10^{-13} cm^2 s^{-1} (lithiation) and 1.8×10^{-12} cm^2 s^{-1} (delithiation) are achieved at 60 °C (Fig. 3i). Such fast Li^+ diffusivity at different temperatures (Table S2) is verified by the CV tests (Fig. S8) [34], which is undoubtedly attributed to the open and stable layered structure of $NiNb_2O_6$. The temperature increase indeed enhances the electrochemical kinetics, providing a good explanation for the observed variations in the rate performance at 25, − 10, and 60 °C.

© The authors
https://doi.org/10.1007/s40820-024-01497-z

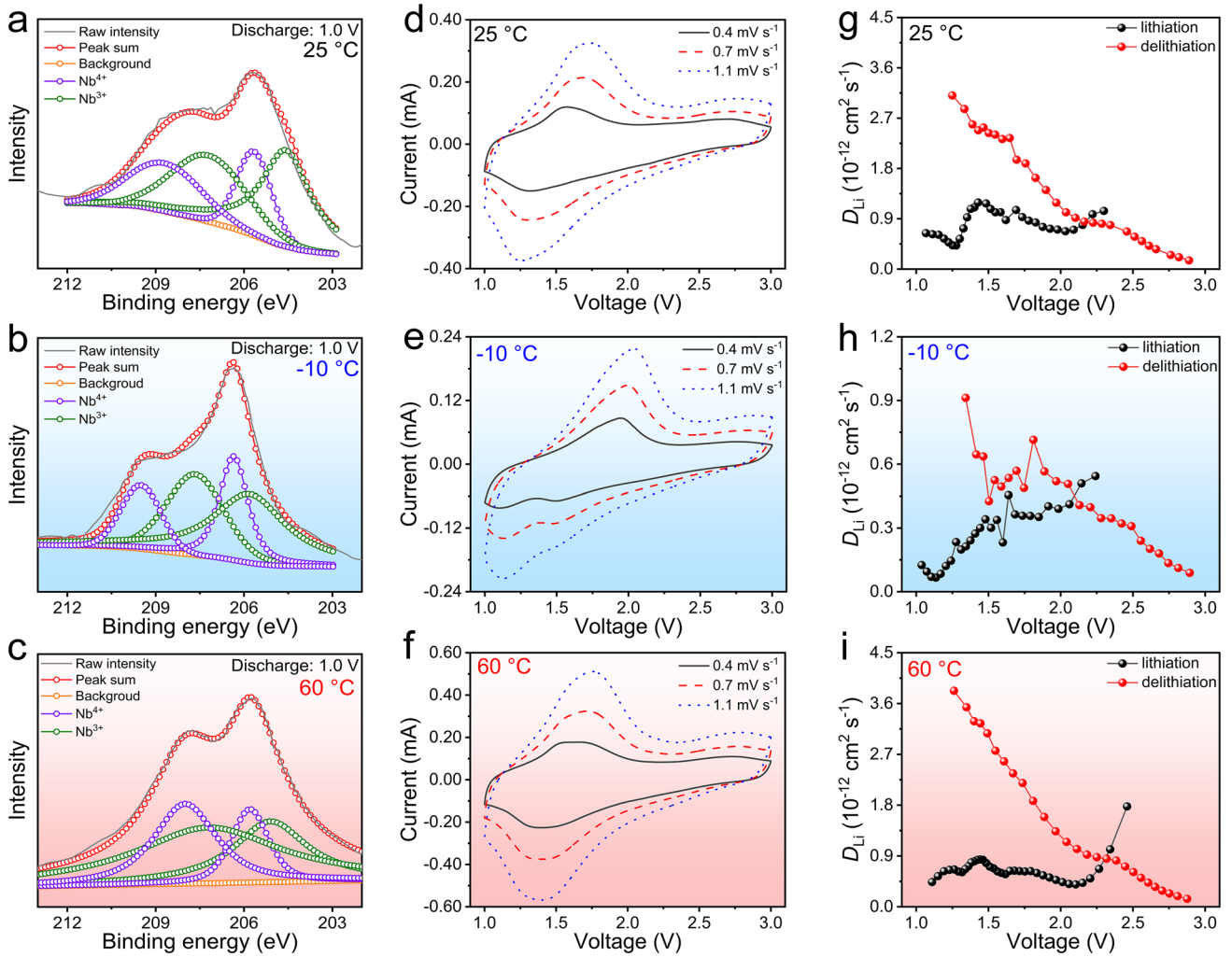

Fig. 3 Redox mechanism and electrochemical kinetics of $NiNb_2O_6$ fibers. Ex-situ Nb-3*d* XPS spectra at discharge state (1.0 V): **a** 25, **b** – 10, and **c** 60 °C. CV curves of $NiNb_2O_6$/Li half-cell at different sweep rates: **d** 25, **e** – 10, and **f** 60 °C. Apparent Li^+ diffusion coefficients during lithiation–delithiation: **g** 25, **h** – 10, and **i** 60 °C. (Color figure online)

At – 10//25//60 °C, the capacitive contribution of the $NiNb_2O_6$ fibers increases with increasing the sweep rates, reaching 94%//84%//82% at 1.1 mV s^{-1} (Fig. S6g–i), which indicates a significant contribution of the capacitive process to the Li^+ storage [51]. This significant pseudocapacitive behavior can be rooted in the spacious crystal structure that is highly suitable for Li^+ intercalation, as well as the fiber morphology with a large specific surface area and abundant pores. Since the capacitive process is not limited by solid-state diffusion [52], the capacitive behavior allows for fast charge transport, also benefiting the rate performance of the $NiNb_2O_6$ material [53–58].

3.4 Crystal-Structure Evolutions and "Zero-Strain" Mechanisms

As can be seen from the first-cycle *operando* XRD patterns (Fig. S9a, d), $NiNb_2O_6$ undergoes a phase transformation when discharge to 1.27 V [18], but the new phase retains the same framework as the initial one. During first lithiation, the diffraction peaks at 24.6, 25.4, 30.4, 31.5, 35.6, and 36.2°, which respectively correspond to the (310), (400), (311), (020), (002), and (021) planes of $NiNb_2O_6$, slightly shift towards lower Bragg angles and then slightly shift towards higher Bragg angles at < 1.25 V (Fig. S10a). During subsequent delithiation, these diffraction peaks consistently

shift towards higher Bragg angles, and restore their initial positions. However, during second lithiation without the phase transformation (Fig. 4a, d), all the diffraction peaks consistently shift towards lower Bragg angles, and exhibit the reversible evolution to that during first delithiation, which are highly repeatable during the subsequent cycles (Fig. S11a). Clearly, once the first lithiation process is completed, the crystal structure of $NiNb_2O_6$ becomes very stable.

The lattice-parameter (*a*, *b*, *c*, and *V*) variations of $NiNb_2O_6$ during lithiation–delithiation are determined through Rietveld-refining the *operando* XRD patterns (Figs. 4g, S9g, and S12a). During first lithiation, the *a*, *b*, *c*, and *V* values slowly increase (> 1.25 V) and obviously decrease after the phase transformation (< 1.25 V), and they continue decreasing during first delithiation, which match well with the diffraction-peak shifts. In the subsequent cycles, the lattice-parameter variations are highly reversible (Fig. S11d), slowly increasing during lithiation and then decreasing during delithiation. The total *a*-, *b*-, *c*-, and *V*-value changes after lithiation are determined for the first time, which are as small as + 0.13%, + 0.27%, + 0.13%, and + 0.53%, respectively. During the *operando* TEM test [18], the tested particles exhibit noticeable strain-fringe movement during lithiation, but the variations in the morphology and volume are negligible (Fig. 5a, b; Video S1). In addition, the *operando*/ex-situ HRTEM and FFT characterizations reveal the unchanged (310) lattice spacing at different lithiation/delithiation states (Fig. 5c–f), which are in good agreement with the *operando* XRD characterizations. Importantly, the ex-situ XRD pattern of the $NiNb_2O_6$ electrode after 100 cycles reveals that all the XRD peaks are well maintained (Fig. S13), demonstrating the "zero-strain" characteristic of $NiNb_2O_6$ during long-term cycling.

At − 10 °C, the variations of the *operando* XRD patterns are highly reversible during all the cycles (no phase transformation), and the peak-shift amplitudes are smaller than that at 25 °C (Figs. 4b, e and S9b, e). The maximum *a*-, *b*-, *c*-, and *V*-value changes remain as small as + 0.21%, + 0.23%, + 0.06%, and + 0.51%, respectively (Fig. S9h). In contrast, at 60 °C, the amplitudes of the peak shifts and the variations in the lattice parameters are larger than those at 25 °C (Figs. 4c, f; S9c, f; S10b; and S12b) due to more Li^+ ions intercalated at the high temperature. The maximum changes of the *a*, *b*, *c*, and *V* values slightly increase to + 0.18%, + 0.44%, + 0.15%, and + 0.74%, respectively (Fig. 4i). Therefore, the "zero-strain" characteristic of $NiNb_2O_6$, with the smallest unit-cell-volume change among the known niobates (Table S3), is clearly identified in a broad temperature range, which well explains the excellent cyclability of our $NiNb_2O_6$ material at various temperatures.

The "zero-strain" mechanism of $NiNb_2O_6$ is systematically investigated through *operando* XRD combined with Rietveld refinements. It is found that the movement of the Ni and Nb ions is negligible throughout the electrochemical reaction. During initial lithiation (> 1.3 V) at 25 °C, the adjacent O ions at the $8d_1$ (or $8d_3$) positions approach each other, while the adjacent O ions at the $8d_2$ position move away from each other (Fig. 6a, b and Tables S5, S6), resulting in longer M–O ($8d_1$) bonds, longer M–O ($8d_3$) bonds, shorter M–O ($8d_2$) bonds (M represents Ni or Nb, Table S9), and a 0.23% expansion of the unit-cell volume. During the phase transformation (~ 1.27 V), the three types of O ions suddenly move, but the M–O bonds maintain their initial change trends and the unit-cell volume further expands by 0.23% (Fig. 6b). After the phase transformation (< 1.25 V), the O^{2-} ($8d_1$) and O^{2-} ($8d_2$) ions move to the directions opposite to their initial ones (Fig. 6c), leading to shorter M–O ($8d_1$) bonds, longer M–O ($8d_2$) bonds, and a unit-cell-volume shrinkage (− 0.13%, Fig. 6d and Tables S7, S8). At 1.0 V, the NiO_6 octahedra expand by 4.93%, while the NbO_6 octahedra shrink by 2.23% (Table S10). During first delithiation, the adjacent O ($8d_1$ or $8d_3$) ions move away from each other, while the adjacent O ($8d_2$) ions approach each other, gradually recovering the initial state (Fig. 6a, d). During subsequent lithiation // delithiation, and the movement of O ion, M–O bond lengths, and polyhedron-volume changes exhibit reversible//identical variations compared to those during first delithiation. At − 10 °C, no sudden ion movement (no phase transformation) is observed, and the ion movement amplitudes and the M–O bond changes are smaller (Fig. S14 and Tables S12–S14). Consequently, the volume changes of the NiO_6 (+ 2.74%) and NbO_6 (− 0.83%) octahedra are also smaller (Table S15). In contrast, at 60 °C, the ion movement amplitudes and the M–O bond changes become larger, causing larger NiO_6 (+ 6.21%) and NbO_6 (− 3.05%) octahedron-volume changes (Fig. S15 and Tables S17–S22). At all these three temperatures, the volume-expansion percentages of the NiO_6 octahedra are always roughly twice the volume-shrink percentages of the NbO_6 octahedra. Since the ratio of the NiO_6 and NbO_6 octahedra is 1:2 in the $NiNb_2O_6$ lattice, the expansion of the NiO_6 octahedra almost completely offsets the shrinkage of the NbO_6 octahedra through the reversible

© The authors https://doi.org/10.1007/s40820-024-01497-z

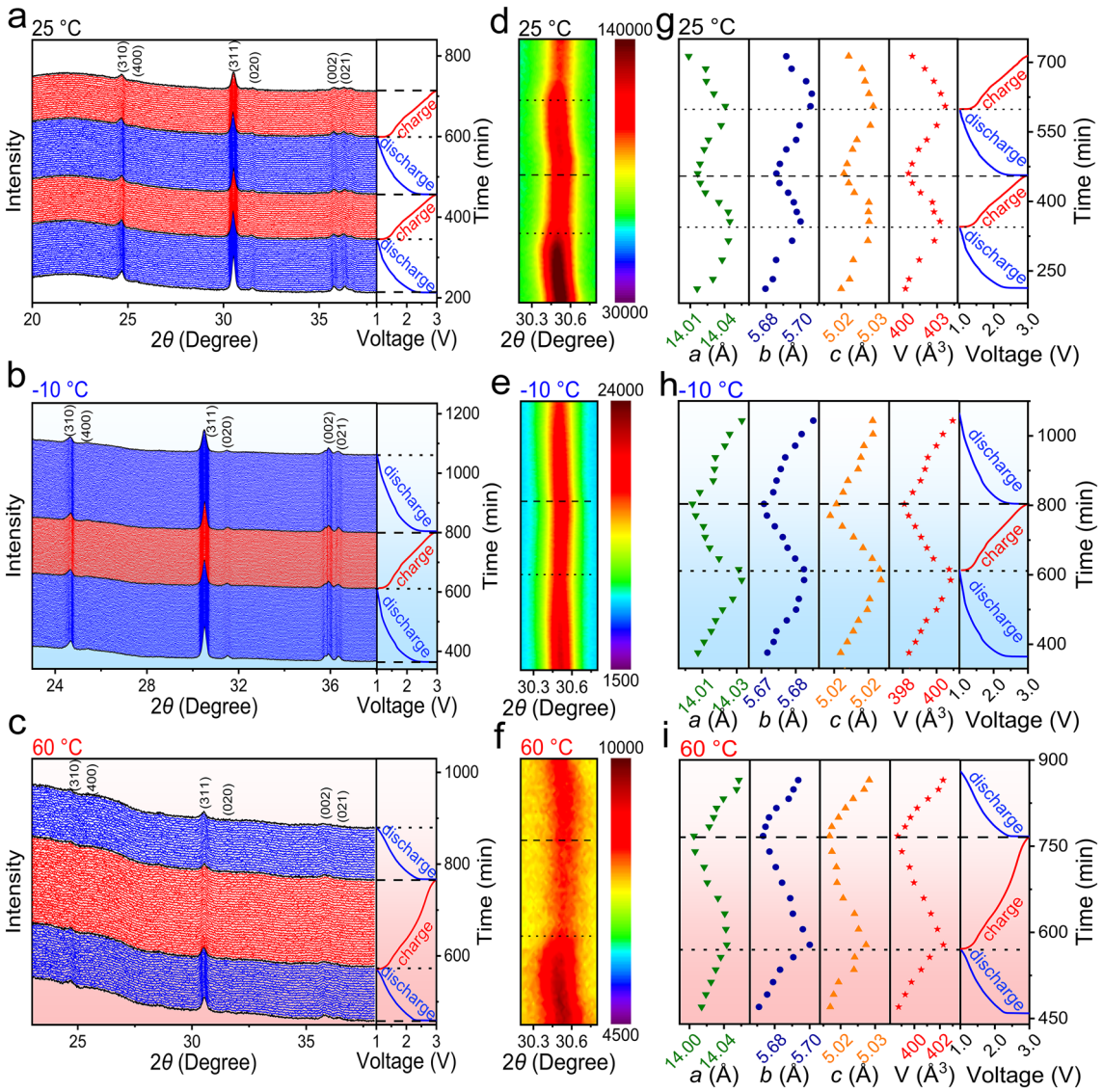

Fig. 4 *Operando* XRD characterizations of $NiNb_2O_6$ fibers within 1.0–3.0 V (second discharge to third charge at 0.5C and 25 °C, second discharge to third discharge at 0.1C and − 10 °C, and second discharge to third discharge at 0.5C and 60 °C). *Operando* XRD patterns of $NiNb_2O_6$/Li half-cell with GCD curves: **a** 25, **b** − 10, and **c** 60 °C. 2D *operando* XRD patterns enlarged within 30.3–30.7°: **d** 25, **e** − 10, and **f** 60 °C. Variations in lattice parameters of $NiNb_2O_6$ during discharge–charge: **g** 25, **h** − 10, and **i** 60 °C. (Color figure online)

O movement, which is the "zero-strain" mechanism of $NiNb_2O_6$ in the broad temperature range. Undoubtedly, the electrochemical inactive NiO_6 layers with superior volume-accommodation capability play the key role in achieving "zero-strain".

4 Conclusions

$NiNb_2O_6$ fibers constructed by nanosized primary particles (50–100 nm) are explored as an all-climate anode material with comprehensively good Li^+-storage properties. This new $NiNb_2O_6$ material exhibits a high electronic conductivity (2.2×10^{-8} S cm^{-1}), large Li^+ diffusion coefficient (averaging at 1.1×10^{-12}//6.1×10^{-13}//1.3×10^{-12} cm^2 s^{-1} at 25// − 10//60 °C), and significant pseudocapacitive

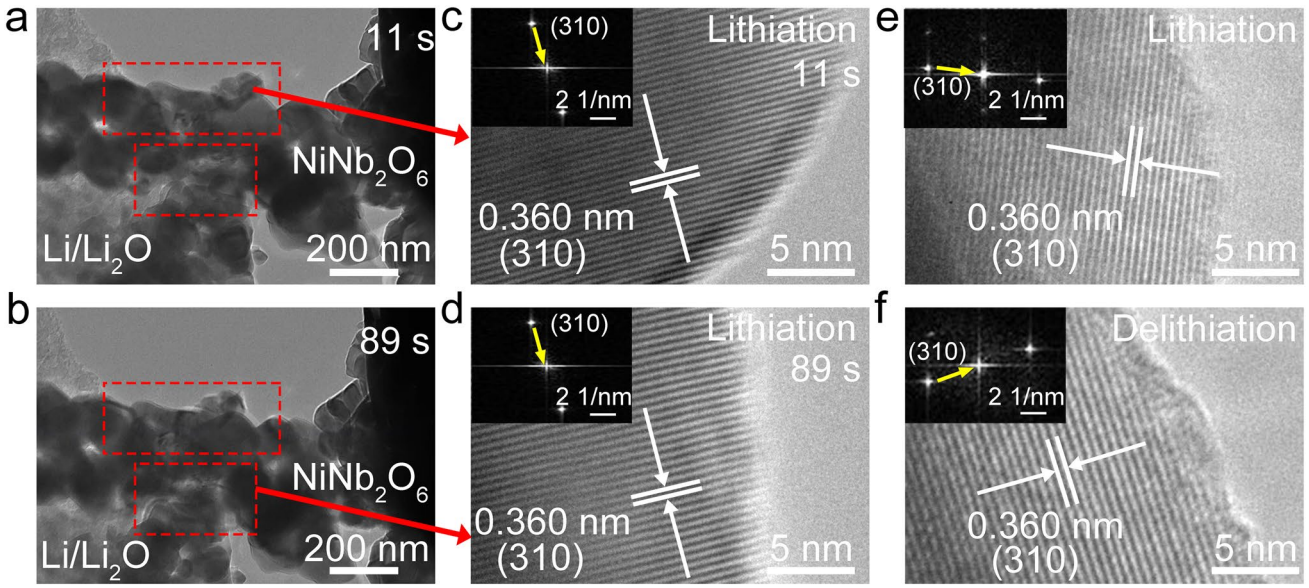

Fig. 5 *Operando* and ex-situ TEM examinations of $NiNb_2O_6$. *Operando* TEM images of Li^+ insertion in $NiNb_2O_6$: **a** 11 and **b** 89 s. *Operando* HRTEM images (*inset*: *operando* FFT) of $NiNb_2O_6$ recorded at lithiation states: **c** 11 and **d** 89 s. Ex-situ HRTEM images (*inset*: ex-situ FFT) of $NiNb_2O_6$: **e** lithiation (1.0 V) and **f** delithiation (3.0 V) states

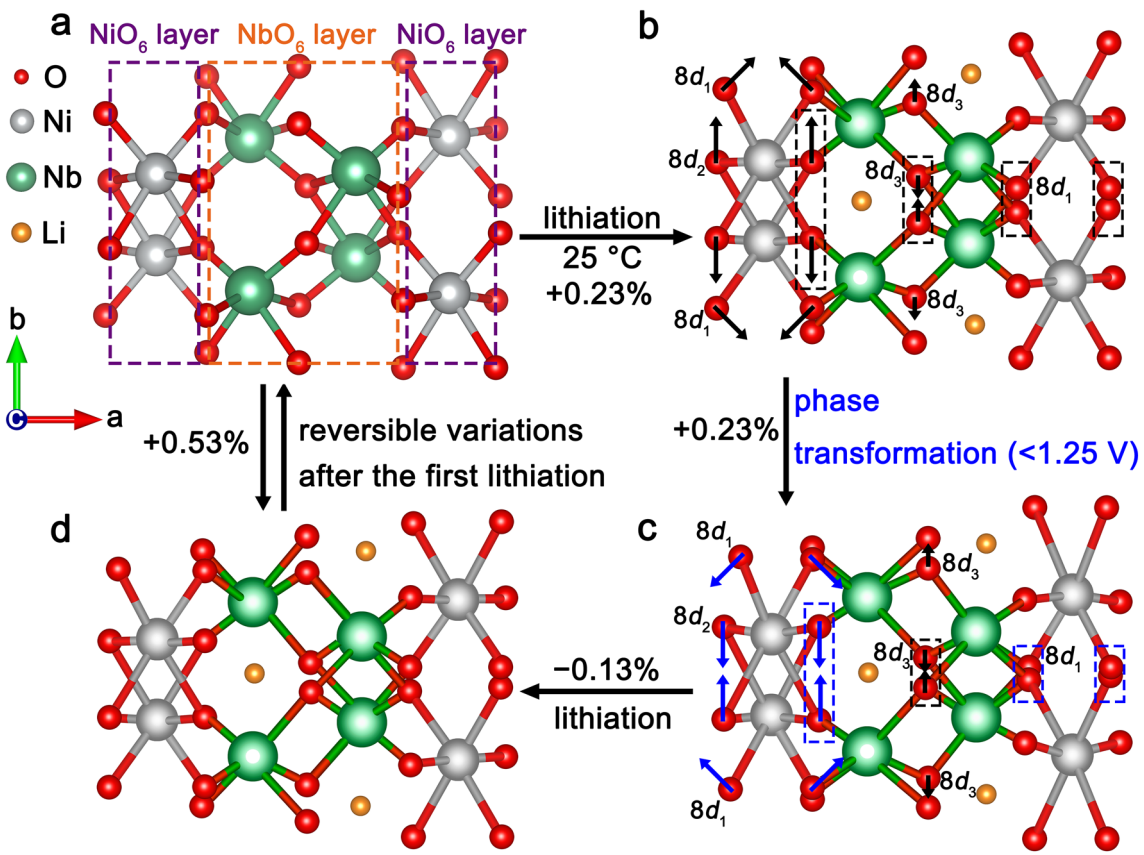

Fig. 6 "Zero-strain" mechanism of $NiNb_2O_6$ at 25 °C. Movement of ions from **a** initial stage to **b** partially lithiated stage, then to **c** phase-transformed stage, and finally to **d** final lithiated stage. Li, Ni, Nb, and O are colored by orange, grey, green, and red, respectively. Arrow lengths indicate movement distances. (Color figure online)

© The authors
https://doi.org/10.1007/s40820-024-01497-z

behavior (94%//84%//82% capacitive contribution at 1.1 mV s^{-1} and 25//−10//60 °C), leading to a large reversible capacity (300//184//318 mAh g^{-1} at 0.1C and 25//−10//60 °C) and outstanding rate performance (10 to 0.5C capacity percentage of 64.3%//50.0%//65.4% at 25//−10//60 °C) in a broad temperature range. The inactive NiO_6 layers, which surround the active NbO_6 layers, effectively accommodate the NbO_6-volume change. The almost completely opposite volume changes of the NiO_6 and NbO_6 octahedra are achieved through the reversible O movement, leading to the "zero-strain" behavior of $NiNb_2O_6$ with minor unit-cell-volume change (0.53%//0.51%//0.74% at 25//−10//60 °C) and excellent cyclability (90.1%//99.2%//92.3% capacity retention after 1000//2000//1000 cycles at 10C and 25//−10//60 °C). The insight gained in this work can provide guide for the exploration of high-performance energy-storage materials working at harsh temperatures.

Acknowledgements This work was supported by the National Natural Science Foundation of China (51762014, 52231007, 12327804, T2321003, 22088101), and in part by the National Key Research Program of China under Grant 2021YFA1200600.

Author Contributions Yan Zhao: Investigation, original draft writing. Qiang Yuan, Liting Yang, Guisheng Liang, Yifeng Cheng: Investigation, visualization. Limin Wu: Review, supervision. Chunfu Lin: Conceptualization, original draft writing, funding acquisition, review, supervision. Renchao Che: Funding acquisition, review, supervision.

Declarations

Conflict of interest The authors declare no interest conflict. They have no known competing financial interests or personal relationships that could have appeared to influence the work reported in this paper.

Open Access This article is licensed under a Creative Commons Attribution 4.0 International License, which permits use, sharing, adaptation, distribution and reproduction in any medium or format, as long as you give appropriate credit to the original author(s) and the source, provide a link to the Creative Commons licence, and indicate if changes were made. The images or other third party material in this article are included in the article's Creative Commons licence, unless indicated otherwise in a credit line to the material. If material is not included in the article's Creative Commons licence and your intended use is not permitted by statutory regulation or exceeds the permitted use, you will need to obtain permission directly from the copyright holder. To view a copy of this licence, visit http://creativecommons.org/licenses/by/4.0/.

Supplementary Information The online version contains supplementary material available at https://doi.org/10.1007/s40820-024-01497-z.

References

1. J. Xu, J. Zhang, T.P. Pollard, Q. Li, S. Tan et al., Electrolyte design for Li-ion batteries under extreme operating conditions. Nature **614**, 694–700 (2023). https://doi.org/10.1038/s41586-022-05627-8
2. T.M.M. Heenan, I. Mombrini, A. Llewellyn, S. Checchia, C. Tan et al., Mapping internal temperatures during high-rate battery applications. Nature **617**, 507–512 (2023). https://doi.org/10.1038/s41586-023-05913-z
3. T. Liu, J. Liu, L. Li, L. Yu, J. Diao et al., Origin of structural degradation in Li-rich layered oxide cathode. Nature **606**, 305–312 (2022). https://doi.org/10.1038/s41586-022-04689-y
4. C.-Y. Wang, T. Liu, X.-G. Yang, S. Ge, N.V. Stanley et al., Fast charging of energy-dense lithium-ion batteries. Nature **611**, 485–490 (2022). https://doi.org/10.1038/s41586-022-05281-0
5. G. Wang, G. Wang, L. Fei, L. Zhao, H. Zhang, Structural engineering of anode materials for low-temperature lithium-ion batteries: mechanisms, strategies, and prospects. Nano-Micro Lett. **16**, 150 (2024). https://doi.org/10.1007/s40820-024-01363-y
6. Y. Feng, L. Zhou, H. Ma, Z. Wu, Q. Zhao et al., Challenges and advances in wide-temperature rechargeable lithium batteries. Energy Environ. Sci. **15**, 1711–1759 (2022). https://doi.org/10.1039/d1ee03292e
7. W. Zhang, D.-H. Seo, T. Chen, L. Wu, M. Topsakal et al., Kinetic pathways of ionic transport in fast-charging lithium titanate. Science **367**, 1030–1034 (2020). https://doi.org/10.1126/science.aax3520
8. J. Hou, M. Yang, D. Wang, J. Zhang, Fundamentals and challenges of lithium ion batteries at temperatures between –40 and 60 °C. Adv. Energy Mater. **10**, 1904152 (2020). https://doi.org/10.1002/aenm.201904152
9. M.-T.F. Rodrigues, G. Babu, H. Gullapalli, K. Kalaga, F.N. Sayed et al., A materials perspective on Li-ion batteries at extreme temperatures. Nat. Energy **2**, 17108 (2017). https://doi.org/10.1038/nenergy.2017.108
10. S.R. Sivakkumar, J.Y. Nerkar, A.G. Pandolfo, Rate capability of graphite materials as negative electrodes in lithium-ion capacitors. Electrochim. Acta **55**, 3330–3335 (2010). https://doi.org/10.1016/j.electacta.2010.01.059
11. T. Waldmann, M. Wilka, M. Kasper, M. Fleischhammer, M. Wohlfahrt-Mehrens, Temperature dependent ageing mechanisms in lithium-ion batteries–a post-mortem study. J. Power. Sources **262**, 129–135 (2014). https://doi.org/10.1016/j.jpowsour.2014.03.112
12. C. Lv, C. Lin, X.S. Zhao, Rational design and synthesis of nickel niobium oxide with high-rate capability and cycling

stability in a wide temperature range. Adv. Energy Mater. **12**, 2102550 (2022). https://doi.org/10.1002/aenm.202102550

13. S. Weng, G. Yang, S. Zhang, X. Liu, X. Zhang et al., Kinetic limits of graphite anode for fast-charging lithium-ion batteries. Nano-Micro Lett. **15**, 215 (2023). https://doi.org/10.1007/s40820-023-01183-6
14. A. Gupta, A. Manthiram, Designing advanced lithium-based batteries for low-temperature conditions. Adv. Energy Mater. **10**, 2001972 (2020). https://doi.org/10.1002/aenm.202001972
15. B. Zhao, R. Ran, M. Liu, Z. Shao, A comprehensive review of $Li_4Ti_5O_{12}$-based electrodes for lithium-ion batteries: the latest advancements and future perspectives. Mater. Sci. Eng. R. Rep. **98**, 1–71 (2015). https://doi.org/10.1016/j.mser.2015.10.001
16. G. Zhu, K. Wen, W. Lv, X. Zhou, Y. Liang et al., Materials insights into low-temperature performances of lithium-ion batteries. J. Power. Sources **300**, 29–40 (2015). https://doi.org/10.1016/j.jpowsour.2015.09.056
17. E. Pohjalainen, T. Rauhala, M. Valkeapää, J. Kallioinen, T. Kallio, Effect of $Li_4Ti_5O_{12}$ particle size on the performance of lithium ion battery electrodes at high C-rates and low temperatures. J. Phys. Chem. C **119**, 2277–2283 (2015). https://doi.org/10.1021/jp509428c
18. W. Wang, Q. Zhang, T. Jiang, S. Li, J. Gao et al., Conductive $LaCeNb_6O_{18}$ with a very open A-site-cation-deficient perovskite structure: a fast- and stable-charging Li^+-storage anode compound in a wide temperature range. Adv. Energy Mater. **12**, 2200656 (2022). https://doi.org/10.1002/aenm.202200656
19. S. Li, J. Gao, Y. Ou, X. Liu, L. Yang et al., Temperature effects on electrochemical energy-storage materials: a case study of yttrium niobate porous microspheres. Small **19**, e2303763 (2023). https://doi.org/10.1002/smll.202303763
20. P. Cui, P. Zhang, X. Chen, X. Chen, T. Wan et al., Oxygen defect and Cl–doped modulated $TiNb_2O_7$ compound with high rate performance in lithium-ion batteries. ACS Appl. Mater. Interfaces **15**, 43745–43755 (2023). https://doi.org/10.1021/acsami.3c08524
21. M. Su, M. Li, X. Long, Y. Lei, X. Chen et al., Insight into the effect of Cu^{2+} doping on $Cu_xNb_{2-x}O_{5-3/2x}$ for high-power lithium-ion batteries. ACS Sustain. Chem. Eng. **11**, 14761–14772 (2023). https://doi.org/10.1021/acssuschemeng.3c04461
22. K.J. Griffith, K.M. Wiaderek, G. Cibin, L.E. Marbella, C.P. Grey, Niobium tungsten oxides for high-rate lithium-ion energy storage. Nature **559**, 556–563 (2018). https://doi.org/10.1038/s41586-018-0347-0
23. J.M. Sieffert, C.J. Lang, S. Bazylevych, S. Jia, E. McCalla, The Nb–Ti–W–O system as safe high-power anodes for Li-ion batteries. J. Mater. Chem. A **12**, 1429–1437 (2024). https://doi.org/10.1039/D3TA06224D
24. Z. Wu, G. Liang, W. Kong Pang, J. Zou, W. Zhang et al., Structural distortion in the Wadsley-Roth niobium molybdenum oxide phase triggering extraordinarily stable battery performance. Angew. Chem. Int. Ed. **63**, e202317941 (2024). https://doi.org/10.1002/anie.202317941
25. Y. Ahn, T. Li, S. Huang, Y. Ding, S. Hwang et al., Mixed-phase niobium oxide as a durable and ultra-fast charging anode for high-power lithium-ion batteries. Adv. Funct. Mater. **34**, 2310853 (2024). https://doi.org/10.1002/adfm.202310853
26. X. Ding, J. Lin, H. Huang, B. Zhao, X. Xiong, Competitive redox chemistries in vanadium niobium oxide for ultrafast and durable lithium storage. Nano-Micro Lett. **15**, 195 (2023). https://doi.org/10.1007/s40820-023-01172-9
27. W. Wu, M. Liu, Y. Pei, W. Li, W. Lin et al., Unprecedented superhigh-rate and ultrastable anode for high-power battery via cationic disordering. Adv. Energy Mater. **12**, 2201130 (2022). https://doi.org/10.1002/aenm.202201130
28. M. Wang, Z. Yao, Q. Li, Y. Hu, X. Yin et al., Fast and extensive intercalation chemistry in Wadsley-Roth phase based high-capacity electrodes. J. Energy Chem. **69**, 601–611 (2022). https://doi.org/10.1016/j.jechem.2022.02.014
29. Y. Yang, J. Huang, Z. Cao, Z. Lv, D. Wu et al., Synchronous manipulation of ion and electron transfer in Wadsley-Roth phase Ti-Nb oxides for fast-charging lithium-ion batteries. Adv. Sci. **9**, e2104530 (2022). https://doi.org/10.1002/advs.202104530
30. M. Su, M. Li, K. He, T. Wan, X. Chen et al., Structure and defect strategy towards high-performance copper niobate as anode for Li-ion batteries. Chem. Eng. J. **455**, 140802 (2023). https://doi.org/10.1016/j.cej.2022.140802
31. Q. Fu, X. Zhu, R. Li, G. Liang, L. Luo et al., A low-strain $V_3Nb_{17}O_{50}$ anode compound for superior Li^+ storage. Energy Storage Mater. **30**, 401–411 (2020). https://doi.org/10.1016/j.ensm.2020.05.012
32. T. Xu, D. Wang, Z. Li, Z. Chen, J. Zhang et al., Electrochemical proton storage: from fundamental understanding to materials to devices. Nano-Micro Lett. **14**, 126 (2022). https://doi.org/10.1007/s40820-022-00864-y
33. Q. Deng, Y. Fu, C. Zhu, Y. Yu, Niobium-based oxides toward advanced electrochemical energy storage: recent advances and challenges. Small **15**, e1804884 (2019). https://doi.org/10.1002/smll.201804884
34. Q. Zhang, S. Ma, W. Wang, S. Gao, Y. Ou et al., "Zero-strain" $K_2SrV_4O_{12}$ as a high-temperature friendly Li^+-storage material. Energy Storage Mater. **52**, 637–645 (2022). https://doi.org/10.1016/j.ensm.2022.08.023
35. G. Liang, L. Yang, Q. Han, G. Chen, C. Lin et al., Conductive $Li_{3.08}Cr_{0.02}Si_{0.09}V_{0.9}O4$ anode material: novel "zero-strain" characteristic and superior electrochemical Li^+ storage. Adv. Energy Mater. **10**, 1904267 (2020). https://doi.org/10.1002/aenm.201904267
36. T.-T. Wei, P. Peng, Y.-R. Ji, Y.-R. Zhu, T.-F. Yi et al., Rational construction and decoration of $Li_5Cr_7Ti_6O_{25}$@C nanofibers as stable lithium storage materials. J. Energy Chem. **71**, 400–410 (2022). https://doi.org/10.1016/j.jechem.2022.04.017
37. R. Xia, K. Zhao, L.-Y. Kuo, L. Zhang, D.M. Cunha et al., Nickel niobate anodes for high rate lithium-ion batteries. Adv. Energy Mater. **12**, 2102972 (2022). https://doi.org/10.1002/aenm.202102972
38. B.H. Toby, *EXPGUI*, a graphical user interface for *GSAS*. J. Appl. Crystallogr. **34**, 210–213 (2001). https://doi.org/10.1107/s0021889801002242

© The authors https://doi.org/10.1007/s40820-024-01497-z

39. W. Huang, C. Yang, N. Miao, C. Lin, W. Xu et al., A novel temperature-dependent electrochemical system for electrode materials for time resolved X-ray diffraction. Scr. Mater. **211**, 114529 (2022). https://doi.org/10.1016/j.scriptamat.2022.114529
40. N. Muralidharan, C.N. Brock, A.P. Cohn, D. Schauben, R.E. Carter et al., Tunable mechanochemistry of lithium battery electrodes. ACS Nano **11**, 6243–6251 (2017). https://doi.org/10.1021/acsnano.7b02404
41. J. Kim, S.H. Jo, S. Bhavaraju, A. Eccleston, S.O. Kang, Low temperature performance of sodium–nickel chloride batteries with NaSICON solid electrolyte. J. Electroanal. Chem. **759**, 201–206 (2015). https://doi.org/10.1016/j.jelechem.2015.11.022
42. C.-H. Shen, R. Gundakaram, R.-S. Liu, H.-S. Sheu, Absence of phase transformation at low temperature in Co-doped $LiMn_2O_4$ samples. J. Chem. Soc. Dalton Trans. **1**, 37–40 (2001). https://doi.org/10.1039/B007120J
43. J.L. Allen, T.R. Jow, J. Wolfenstine, Low temperature performance of nanophase $Li_4Ti_5O_{12}$. J. Power. Sources **159**, 1340–1345 (2006). https://doi.org/10.1016/j.jpowsour.2005.12.039
44. F. Huang, J. Ma, H. Xia, Y. Huang, L. Zhao et al., Capacity loss mechanism of the $Li_4Ti_5O_{12}$ microsphere anode of lithium-ion batteries at high temperature and rate cycling conditions. ACS Appl. Mater. Interfaces **11**, 37357–37364 (2019). https://doi.org/10.1021/acsami.9b14119
45. X. Zhu, J. Xu, Y. Luo, Q. Fu, G. Liang et al., $MoNb_{12}O_{33}$ as a new anode material for high-capacity, safe, rapid and durable Li^+ storage: structural characteristics, electrochemical properties and working mechanisms. J. Mater. Chem. A **7**, 6522–6532 (2019). https://doi.org/10.1039/C9TA00309F
46. S. Li, J. Gao, Y. Ou, W. Wang, Q. Zhang et al., A general strategy to enhance the electrochemical activity and energy density of energy-storage materials through using sintering aids with redox activity: a case study of $Mo_4Nb_{26}O_{77}$. J. Mater. Chem. A **10**, 19953–19962 (2022). https://doi.org/10.1039/D2TA02169B
47. Q. Fu, R. Li, X. Zhu, G. Liang, L. Luo et al., Design, synthesis and lithium-ion storage capability of $Al_{0.5}Nb_{24.5}O_{62}$. J. Mater. Chem. A **7**, 19862–19871 (2019). https://doi.org/10.1039/c9ta04644e
48. M. Liang, Y. Huang, Y. Lin, G. Liang, C. Huang et al., Micro-nano structured VNb_9O_{25} anode with superior electronic conductivity for high-rate and long-life lithium storage. J. Mater. Sci. Technol. **83**, 66–74 (2021). https://doi.org/10.1016/j.jmst.2020.12.018
49. Y. De Luna, N. Bensalah, Mechanochemical synthesis of orthorhombic nickel niobate ($NiNb_2O_6$) as a robust and fast charging anode material for lithium-ion batteries. ACS Appl. Energy Mater. **5**, 7443–7457 (2022). https://doi.org/10.1021/acsaem.2c00935
50. A.J. Bard, L.R. Faulkner, *Electrochemical Methods: Fundamentals and Applications*, vol. 38, 2nd edn. (Wiley, New York, 2001), pp. 1364–1365. https://doi.org/10.1023/A:1021637209564
51. J. Wang, J. Polleux, J. Lim, B. Dunn, Pseudocapacitive contributions to electrochemical energy storage in TiO_2 (anatase) nanoparticles. J. Phys. Chem. C **111**, 14925–14931 (2007). https://doi.org/10.1021/jp074464w
52. V. Augustyn, J. Come, M.A. Lowe, J.W. Kim, P.L. Taberna et al., High-rate electrochemical energy storage through Li^+ intercalation pseudocapacitance. Nat. Mater. **12**, 518–522 (2013). https://doi.org/10.1038/nmat3601
53. L. Yan, X. Rui, G. Chen, W. Xu, G. Zou et al., Recent advances in nanostructured Nb-based oxides for electrochemical energy storage. Nanoscale **8**, 8443–8465 (2016). https://doi.org/10.1039/c6nr01340f
54. H. Jiang, H. Zhang, L. Chen, Y. Hu, C. Li, Nanospace-confinement synthesis: designing high-energy anode materials toward ultrastable lithium-ion batteries. Small **16**, e2002351 (2020). https://doi.org/10.1002/smll.202002351
55. L. Ji, Z. Lin, M. Alcoutlabi, X. Zhang, Recent developments in nanostructured anode materials for rechargeable lithium-ion batteries. Energy Environ. Sci. **4**, 2682–2699 (2011). https://doi.org/10.1039/C0EE00699H
56. Z. Li, M. Han, P. Yu, J. Lin, J. Yu, Macroporous directed and interconnected carbon architectures endow amorphous silicon nanodots as low-strain and fast-charging anode for lithium-ion batteries. Nano-Micro Lett. **16**, 98 (2024). https://doi.org/10.1007/s40820-023-01308-x
57. Y. Lu, R. Zhou, N. Wang, Y. Yang, Z. Zheng et al., Engineer nanoscale defects into selective channels: MOF-enhanced Li^+ separation by porous layered double hydroxide membrane. Nano-Micro Lett. **15**, 147 (2023). https://doi.org/10.1007/s40820-023-01101-w
58. J. Ren, Z. Wang, P. Xu, C. Wang, F. Gao et al., Porous Co_2VO_4 nanodisk as a high-energy and fast-charging anode for lithium-ion batteries. Nano-Micro Lett. **14**, 5 (2021). https://doi.org/10.1007/s40820-021-00758-5

Publisher's Note Springer Nature remains neutral with regard to jurisdictional claims in published maps and institutional affiliations.